

# Excitons in Phosphorene: A Semi-Analytical Perturbative Approach

J. C. G. Henriques<sup>1</sup> and N. M. R. Peres<sup>1,2</sup>

<sup>1</sup>*Department and Centre of Physics, and QuantaLab,  
University of Minho, Campus of Gualtar, 4710-057, Braga, Portugal and*

<sup>2</sup>*International Iberian Nanotechnology Laboratory (INL),  
Av. Mestre Jose Veiga, 4715-330, Braga, Portugal*

(Dated: July 28, 2021)

In this paper we develop a semi-analytical perturbation-theory approach to the calculation of the energy levels (binding energies) and wave functions of excitons in phosphorene. Our method gives both the exciton wave function in real and reciprocal spaces with the same ease. This latter aspect is important for the calculation of the nonlinear optical properties of phosphorene. We find that our results are in agreement with calculations based both on the Bethe-Salpeter equation and on Monte Carlo simulations, which are computationally much more demanding. Our approach thus introduces a simple, viable, and accurate method to address the problem of excitons in anisotropic two-dimensional materials.

## I. INTRODUCTION

Although black phosphorus was first obtained in 1914, over a century ago, few research was developed around this material throughout most part of the twentieth century. In 100 years only around one hundred papers have been written [1]. With the isolation of monolayer graphene in 2004 [2], an intensive study has been made on two-dimensional (2D) materials [3–5]. This opened a new window of opportunity for black phosphorus to show its potential in the form of a few-layer material, named phosphorene. Since 2014, building on the work done on graphene, hexagonal boron nitride (hBN), and transition metal dichalcogenides (TMD's), black phosphorus has been rediscovered [1].

Black phosphorus is the most stable of the phosphorus allotropes, and presents a unique structure when reduced to few layers. Along with graphite, it is one of the few-layer materials composed by a single type of atom, in this case, phosphorus [6]. Unlike graphene, TMD's, and hBN, phosphorene presents a rectangular primitive cell composed of four atoms and the energy gap is located at  $\Gamma$ -point in the Brillouin zone. Also, unlike these other materials, phosphorene presents a highly anisotropic crystallographic structure, as can be seen in Figure 1. The puckering of its structure results in a plethora of exotic properties, examples being the negative Poisson ratio [7] and the existence of intrinsic dichroism [8].

Contrary to what occurs in TMD's, phosphorene presents a direct band gap in both monolayer and bulk forms. The values of the quasi-particle gap range from 0.3 eV (in bulk) to 2.0 eV (in monolayer) [9, 10]. Besides that, phosphorene's band gap can be finely tuned through the number of layers. The increase of the gap as the material is thinned can be understood in terms of a concomitant increase of the quantum confinement in the perpendicular direction to the stacking plane of the layers. Studies have also reported high mobility and high on-off current ratio in field-effect transistors [11–13]. This set of characteristics makes phosphorene a desirable

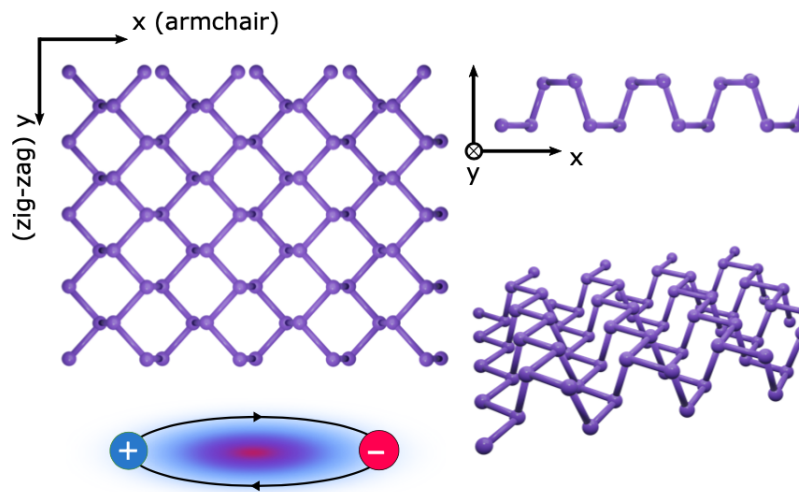


Figure 1. (Color online) Schematic representation of phosphorene from three different perspectives: top view, side view, and in perspective. With this, the anisotropic nature of phosphorene's crystal lattice becomes clear. Also at the bottom left of the image an artistic view of phosphorene anisotropic excitons is given.

material for electronic and optical applications [14–16].

Like many others 2D materials (graphene being a notable exception), excitons dominate phosphorene's optical properties. Experimental works have reported highly anisotropic and tightly bound excitons, with binding energies up to 900 meV [17]. A large binding energy allows for stable excitons with increased lifetimes. These are important properties for future applications in light transport and optically driven quantum computing [6]. Due to the importance of optical applications involving phosphorene, in this paper we focus our attention on the study of exciton binding energies and wave function anisotropy, characteristics of this 2D material. Our approach follows a simple, yet effective, path. Instead of solving the Bethe Salpeter equation starting from *ab-initio* calculations [18], which is computationally demanding, we follow the path of solving the anisotropic Wannier equation.

This approach has been shown, in the context of TMD's in strong magnetic fields, to produce binding energies in full agreement with the solution of the Bethe-Salpeter equation [19]. As we will see, our approach proposes a semi-analytical form for the wave function of the excitons up to a set of numerical coefficients determined from the solution of a generalized eigenvalue problem.

This paper is organized as follows: In the next section we present the model Hamiltonian, and transform it in order to separate our problem in two parts: an unperturbed Hamiltonian, which has cylindrical symmetry, and a perturbation one, which includes the lattice anisotropy information. Next, we introduce a simple semi-analytical method that allows us to solve the cylindrical symmetric part of our problem. In Sec. III we present the necessary formalism to compute the effect of perturbations breaking the cylindrical symmetry. Afterwards, in Sec. IV, we compute the exciton binding energies and wave functions for three different scenarios: phosphorene encapsulated in hBN, phosphorene on a substrate of silicon oxide (SiO<sub>2</sub>), and phosphorene in freestanding form. Finally we compare our results to values obtained in other works, finding a good agreement.

## II. MODEL HAMILTONIAN

We start this section introducing the effective Hamiltonian that will be used throughout the text to describe the exciton dynamics in black phosphorus; it reads

$$H = \frac{p_x^2}{2\mu_x} + \frac{p_y^2}{2\mu_y} + V(r). \quad (1)$$

This is a center of mass Hamiltonian, composed of a kinetic (first and second) and potential (last) terms. Since black phosphorus is a highly anisotropic material there are two different reduced masses in the  $x$  and  $y$  directions, thus leading to two different contributions to the kinetic terms, one for each direction in momentum space. The reduced masses are defined as

$$\mu_{x/y} = \frac{m_{x/y} M_{x/y}}{m_{x/y} + M_{x/y}}, \quad (2)$$

with  $m_{x/y}$  and  $M_{x/y}$  being the effective masses of electrons and holes, respectively, in the  $x/y$  direction. The potential term  $V(r)$  corresponds to the Rytova-Keldysh potential [20, 21], and is given by

$$V(r) = -\frac{e^2}{4\pi\epsilon_0} \frac{\pi}{2} \frac{1}{r_0} \left[ \mathbf{H}_0\left(\frac{\kappa r}{r_0}\right) - Y_0\left(\frac{\kappa r}{r_0}\right) \right], \quad (3)$$

where  $r_0 \sim d\epsilon/2$ , with  $d$  and  $\epsilon$  the thickness and dielectric function of the 2D material, respectively;  $\kappa = (\epsilon_1 + \epsilon_2)/2$  is the mean dielectric function of the media surrounding the 2D material (either different or equal on each side of the material);  $\mathbf{H}_0(x)$  is the Struve function of zero order and  $Y_0(x)$  is the Bessel function of zero order of

the second kind. This potential is the solution of the Poisson equation for a thin film embed in a medium.

With the intent of passing the anisotropy from the kinetic term to the potential energy  $V(r)$  term, we follow the change of variables proposed by Rodin *et al.* in Ref.[22]:

$$\sqrt{\frac{\mu_{x/y}}{2\bar{\mu}m_0}} x/y = X/Y, \quad \bar{\mu} = \frac{\mu_x \mu_y}{\mu_x + \mu_y} \frac{1}{m_0}. \quad (4)$$

Performing this change of variables, the Hamiltonian (1) acquires the form

$$H = -\frac{\hbar^2}{4\bar{\mu}m_0} \nabla^2 + V(R\sqrt{1 + \beta \cos(2\theta)}), \quad (5)$$

where the kinetic term has now the usual form, albeit with a different mass,  $\beta = (\mu_y - \mu_x)/(\mu_y + \mu_x)$ , and  $\theta$  is the in-plane polar angle. The parameter  $\beta$  characterizes the degree of anisotropy. The larger it is the more anisotropic the system is. The new variable  $R$  is defined as  $R = \sqrt{X^2 + Y^2}$ . We see that this variable change produces the desired effect, that is, the anisotropy is now present in the potential, and the kinetic term takes the usual form of an isotropic center of mass system, with reduced mass equal to  $2\bar{\mu}m_0$ . From now on we will work in this new coordinate system, and only return to the original  $x$  and  $y$  coordinates when plots are presented and concrete values for averages of distances are computed. To avoid misunderstandings we will warn the reader when confusion may arise.

The main advantage of working with the Hamiltonian in this form is two fold: (i) the unperturbed Hamiltonian has cylindrical symmetry and (ii) we can now expand the potential energy term in powers of  $\beta$ , allowing us to separate Eq. (5) into an unperturbed Hamiltonian and an additional perturbative potential energy. Taylor expanding the potential energy up to order  $\beta^2$ , we obtain

$$H = -\frac{\hbar^2}{4\bar{\mu}m_0} \nabla^2 + V(R) + \frac{1}{2} R \cos(2\theta) \frac{dV}{dR} \beta + \cos^2(2\theta) \frac{1}{8} \left( R^2 \frac{d^2 V}{dR^2} - R \frac{dV}{dR} \right) \beta^2 + \mathcal{O}(\beta^3). \quad (6)$$

We can now divide our problem into two different stages: (a) solving the unperturbed problem, whose Hamiltonian consists of the first two terms in Eq. (6); (b) computing the corrections introduced by the terms proportional to  $\beta$  and  $\beta^2$ .

In order to solve the unperturbed problem we will introduce a semi-analytical method that has already shown excellent results in a previous work [23]. The quasi-analytical nature of this method makes it less computationally demanding than other approaches, and much simpler to work with when compared to fully numerical calculations which diagonalize the Bethe-Salpeter equation starting from *ab-initio* calculations. Inspired by the analytical solution of the 2D hydrogen atom [24], we write

the exciton wave function as

$$\psi_{\nu}^{(0)}(\mathbf{r}) = \mathcal{A}_{\nu} \sum_{j=1}^N c_j^{\nu} e^{im\theta} r^{|m|} e^{-\zeta_j r}, \quad (7)$$

where  $e^{im\theta} r^{|m|}$  follows from the eigenfunctions of the  $z$ -component of the angular momentum and from the radial behavior of the wave function near the origin, for  $m = 0, \pm 1, \pm 2, \dots$ , the magnetic quantum number; the exponential term (Slater basis)  $e^{-\zeta_j r}$  describes the decay of the radial part of the wave function far from the origin, with a decay rate determined by the parameter  $\zeta_j$ ; the coefficients  $c_j^{\nu}$  weight the different terms in the sum and  $\mathcal{A}_{\nu}$  is a normalization constant given by

$$\mathcal{A}_{\nu} = \sqrt{\frac{1}{2\pi\mathcal{S}_{\nu}}}, \quad (8)$$

with  $\mathcal{S}_{\nu} = \sum_{j=1}^N \sum_{j'=1}^N c_j^{\nu*} c_{j'}^{\nu} (\zeta_j + \zeta_{j'})^{-2-2|m|} \Gamma(2|m|+2)$ , and where  $\Gamma(x)$  is the Gamma function. The index  $\nu$  encodes both the principal ( $n$ ) and the angular ( $m$ ) quantum numbers. An additional advantage of this method is that the matrix elements of both the kinetic operator and the electron-electron interaction do not mix different  $m$  values and, therefore, the eigenvalue problem is block diagonal in the angular momentum space. In this work, and contrary to Ref. [23], we opt to work with a Slater basis instead of a Gaussian one since this choice allows us to obtain more accurate results using fewer terms in Eq. (7). Contrary to the Gaussian basis, we have found that the Slater basis requires more care in the choice of parameters defining the grid of  $\zeta_j$ 's (see below).

Using the proposed wave function and computing the matrix elements of the kinetic and potential operators (see Appendix), the generalized eigenvalue problem, whose numerical solution gives the coefficients  $c_j^{\nu}$  and the *unperturbed* binding energies  $E_{\nu}^{(0)}$ , acquires the form

$$\sum_{j=1}^N [H(\zeta_i, \zeta_j) - S(\zeta_i, \zeta_j) E_{\nu}^{(0)}] c_j^{\nu} = 0, \quad (9)$$

where  $H(\zeta_i, \zeta_j)$  is the Hamiltonian kernel and  $S(\zeta_i, \zeta_j)$  is the superposition kernel. Both kernels have analytical expressions that are given in the Appendix. The superposition kernel differs from a Kronecker- $\delta$  since the Slater basis is not orthogonal. Equation (9) was first introduced in nuclear physics and is termed the Griffin-Hill-Wheeler equation [25]. The key aspect of this method is the sensible choice of the parameters  $\zeta_j$ . A choice not so well known is the use of a logarithmic grid of  $\zeta$ 's according to the rule given in Ref.[26]

$$\Omega = \frac{\ln \zeta}{A}, \quad A > 1, \quad (10)$$

where the grid  $\Omega$  is composed of equally spaced values in the interval  $[\Omega_{min}, \Omega_{max}]$  and  $A$  is real number typically chosen between 2 and 5. The interval is divided in  $N$  steps.

### III. PERTURBATION THEORY

With the unperturbed problem dealt with, we will use this section to present the necessary formalism to compute the corrections introduced by the perturbation

$$H^{(1)} = \frac{1}{2} R \cos(2\theta) \frac{dV}{dR} \beta + \cos^2(2\theta) \frac{1}{8} \left( R^2 \frac{d^2V}{dR^2} - R \frac{dV}{dR} \right) \beta^2, \quad (11)$$

that is, the remaining terms of the potential expansion given in Eq. (6).

We start noting that the kernel expressions given in the Appendix do not depend on  $m$  but rather on its absolute value  $|m|$ . This means that every state with  $m \neq 0$  will be degenerate, since two states with equal principal quantum number  $n$  and magnetic quantum numbers  $m$  and  $-m$  will have the same kernels, and therefore the same eigenenergies. One thus needs to be careful when computing the energy corrections through perturbation theory, since a separation between degenerate and non-degenerate states must be made.

Starting with the non-degenerate states ( $m = 0$ ), the first-order energy correction is elementary and is given by the matrix element (all the matrix elements in this work are known analytically)

$$E_{\nu}^{(1)} = \langle \psi_{\nu}^{(0)} | H^{(1)} | \psi_{\nu}^{(0)} \rangle, \quad (12)$$

where the superscript (0) indicates that these are unperturbed wave functions, that is, they are the solution of first two terms of Eq. (6). Looking at the wave function given in Eq. (7), especially to its angular dependence, one realizes that the first-order energy correction is zero for the perturbation term proportional to  $\beta$ , since the integral of  $\cos(2\theta)$  between 0 and  $2\pi$  vanishes. Only the  $\beta^2$  portion of the perturbation gives a non-zero result up to first order correction to the unperturbed binding energies.

For the degenerate states, the first-order correction is obtained from the solution of the secular equation

$$\det [H_{\alpha\beta}^{(1)} - E \delta_{\alpha\beta}^{\beta}] = 0, \quad (13)$$

with

$$H_{\alpha\beta}^{(1)} = \langle \psi_{\alpha}^{(0)} | H^{(1)} | \psi_{\beta}^{(0)} \rangle. \quad (14)$$

For clarity sake let us work out a specific case that will be used later in the text. Consider the degenerate states ( $n = 2, m = \pm 1$ ). The energy corrections will be given simply by

$$E^{(1)} = \pm \langle \psi_{2,1}^{(0)} | H^{(1)} | \psi_{2,-1}^{(0)} \rangle + \langle \psi_{2,1}^{(0)} | H^{(1)} | \psi_{2,1}^{(0)} \rangle, \quad (15)$$

where the first term will only produce a finite contribution for the perturbation term proportional to  $\beta$ , and the

second term for the term proportional to  $\beta^2$ . The new eigenstates will be superpositions of the original unperturbed states, that is

$$|2p_{x/y}\rangle = \frac{1}{\sqrt{2}} \left( |\psi_{2,1}^{(0)}\rangle \pm |\psi_{2,-1}^{(0)}\rangle \right). \quad (16)$$

This superposition of states is to be expected, since  $m$  is no longer a suitable quantum number, due to the loss of rotational symmetry in the original problem.

To further improve the energy eigenvalues, we compute the second-order correction for the non-degenerate states, only considering the term of  $H^{(1)}$  linear in  $\beta$ , since we only want corrections up to  $\beta^2$ . This correction reads

$$E_\nu^{(2)} = \sum_{\mu \neq \nu} \frac{\left| \left\langle \psi_\mu^{(0)} \left| \frac{1}{2} R \cos(2\theta) \frac{dV}{dR} \beta \right| \psi_\nu^{(0)} \right\rangle \right|^2}{E_\nu^{(0)} - E_\mu^{(0)}}. \quad (17)$$

Although the sum should cover all the  $\mu$  states different from  $\nu$ , we consider only the dominant term in the sum, that is, that for which the ratio  $|\langle \nu | H^{(1)} | \mu \rangle|^2 / (E_\nu^{(0)} - E_\mu^{(0)})$  has the largest absolute value. Therefore, the exact value for the ground state energy will be slightly more negative than what we actually compute. It is important to note that, once again, the angular dependence of the wave functions plays a crucial role in evaluating the matrix elements, since there will be coupling only between  $\mu$  and  $\nu$  states whose angular functions combine to give  $e^{\pm 2im\theta}$ . Since cosine is an even function, and only the real part of the exponential will couple with  $\cos(2\theta)$ , the sign difference in the complex exponential will not change the matrix element value.

Having determined the binding energies corrections, we proceed to compute the first-order correction to the wave functions, using the relation

$$|\psi_\nu^{(1)}\rangle = \sum_{\mu \neq \nu} \frac{\langle \psi_\mu^{(0)} | H^{(1)} | \psi_\nu^{(0)} \rangle}{E_\nu^{(0)} - E_\mu^{(0)}} |\psi_\mu^{(0)}\rangle, \quad (18)$$

where, and once again, we only consider the dominant term in the sum.

#### IV. RESULTS

In this section we apply the formalism introduced previously to three different cases: phosphorene encapsulated in hBN; phosphorene on a substrate of SiO<sub>2</sub>; and freestanding phosphorene. Due to the similarities between the analysis for these three physical systems, we will give special attention to the case of phosphorene encapsulated in hBN (due to its experimental relevance), and comment on the differences to the other two scenarios.

Let us start applying the semi analytical method introduced in Sec. II to black phosphorus encapsulated in hBN. For this experimental scenario we have  $\kappa = 4.5$ ,

and  $r_0 = 25$  Å [27]. Considering the effective masses of Ref. [28], presented in Table I, one obtains  $\beta = 0.62$ . Using the parameters:  $N = 25$ ,  $A = 5$ , and  $\Omega = [-2, 2]$  we obtain the *unperturbed* binding energies given in Table II. A plot of these binding energies is shown in Figure 2.

	Ref. [27]	Ref. [29]	Ref. [28]
$m_x$	$1.15m_0$	$0.20m_0$	$0.46m_0$
$m_y$	$0.24m_0$	$6.89m_0$	$1.12m_0$
$M_x$	$7.29m_0$	$0.20m_0$	$0.23m_0$
$M_y$	$0.24m_0$	$6.89m_0$	$1.61m_0$
$\beta$	-0.78	0.94	0.62

Table I. Values for the effective masses of electrons ( $m$ ) and holes ( $M$ ) in the  $x$  and  $y$  directions. The masses are presented in terms of  $m_0$ , the bare electron mass. We have used the effective masses of Ref. [28]. We have checked that the binding energy of the  $1s$  exciton, for free standing phosphorene, changed by 6 meV if one uses  $\beta = -0.78$ .

	(1,0)	(2,0)	(2, $\pm 1$ )	(3, $\pm 1$ )	(3, $\pm 2$ )
in hBN	-234	-50	-64	-25	-26
on SiO <sub>2</sub>	-428	-121	-160	-66	-78
Freestanding	-799	-340	-424	-232	-262

Table II. *Unperturbed* exciton binding energies (in meV) obtained using the semi-analytical method described in Sec. II, for phosphorene encapsulated in hBN, on a substrate of SiO<sub>2</sub>, and freestanding. The parenthesis refer to the exciton state ( $n, m$ ). These values were obtained using the  $N = 25$ ,  $A = 5$ , and  $\Omega = [-2, 2]$ . A value of  $r_0 = 25$  Å was considered [27]. As discussed previously, we observe that states with  $m \neq 0$  are degenerate. We also note that, as expected, the binding energies are inferior for the cases with more dielectric screening, that is, higher values of  $\kappa$  ( $\kappa = 1$  for freestanding and  $\kappa = 2.4$  for phosphorene on SiO<sub>2</sub>). Let us stress that the energies given in this table refer to the solution of the Hamiltonian given by the first two terms of Eq. (6); the effect of the perturbation has not yet been considered.

For the cases of black phosphorus on a SiO<sub>2</sub> substrate, and for freestanding black phosphorus, we observed larger binding energies (in absolute value) than when we encapsulate the material in hBN. This is a sensible result, since in these two other cases the effect of dielectric screening is reduced and, as a consequence, the excitons are more tightly bound. Freestanding phosphorene presents the largest exciton binding energies of the lot.

After computing the unperturbed eigenenergies we proceeded to compute the energy corrections as described in Section III. Calculating the first order corrections to the degenerate and non-degenerate states using equations (12) and (15) is a straightforward process. The same cannot be said about the second order corrections, where an

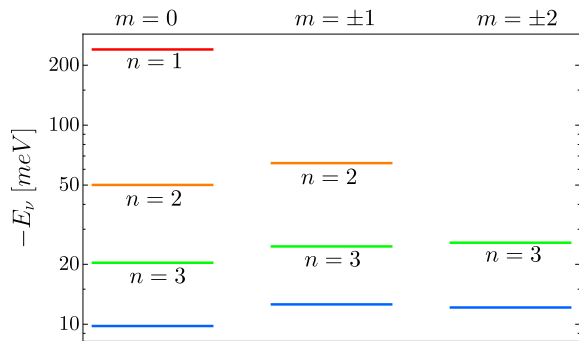


Figure 2. (Color online) Plot in a log-scale of the *unperturbed* exciton binding energies (actually,  $-E_{\text{binding}} = -E_v^{(0)}$ ) for phosphorene encapsulated in hBN. Each column corresponds to a different quantum number  $m$  (0,  $\pm 1$ ,  $\pm 2$ , from left to right), and each color corresponds to a specific quantum number  $n$  (from 1 to 4).

approximation is made when truncating the sum over the different states. As was previously discussed in the text that follows Eq. (17), we only consider the dominant term of the sum. To do this correctly a plot like the one in Fig. 2 is useful, since it allows us to see with clarity which combination of two states is likely to give the largest contribution. States with similar unperturbed binding energies will, in principle, produce a significant contribution to the correction. An example of this is the second correction to the state  $n = 2$ ,  $m = 0$ . Here the dominant term is obtained from the matrix element with the state  $n = 3$ ,  $m = \pm 2$ , giving a correction of around  $-13$  meV. Although this may seem a higher value than expected for a second order correction, looking at Figure 2 it becomes clear that the states  $n = 2$ ,  $m = 0$  and  $n = 3$ ,  $m = \pm 2$  present the smallest difference of the unperturbed binding energies (orange-green), which enhance the weight of this contribution, making it the dominant term to the perturbative sum.

The values we obtained for the corrected ground state binding energy and their comparison to other results from the literature are summarized in Table III. In this table we observe an excellent agreement between our values and the ones given by other references, using different numerical approaches (note, however, that there is a certain degree of dispersion within the values reported by different works). In agreement to what was found in the other works, the three more tightly bound excitons correspond to  $1s$ ,  $2p_y$ , and  $2s$  states. We also emphasize that the proximity between results extends across the three considered combinations of phosphorene and dielectrics.

In Figure 3 we plot the probability density (squared

modulus of the corrected wave functions) for the three more tightly bound excitons of phosphorene encapsulated in hBN. As stated before, these correspond to  $1s$ ,  $2p_y$ , and  $2s$  states, respectively. Although we only show the plots for the case where we encapsulate phosphorene in hBN, the plots obtained for the other two situations are

	in hBN on SiO <sub>2</sub> freestanding		
This work	-256	-449	-825
Ref. [30]	-300	-460	-910
Ref. [27]	-260	-440	-810
Ref. [22]	-220	–	–
Ref. [13]	–	-380	–
Ref. [31]	–	-396	–
Ref. [28]†	–	–	-850
Ref. [17]*	–	–	-900±120
Ref. [32]	–	–	-740
Ref. [18]	–	–	-840
Ref. [33]	–	–	-780
Ref. [34]	–	–	-860
Ref. [35]*	–	–	-762

Table III. Comparison between the *perturbed* ground state exciton binding energy obtained in this work, taking in consideration the effect of the terms in the potential energy proportional to  $\beta$  and  $\beta^2$ , and the ones available in the literature. All energies are given in meV. We report a good agreement between our values and the ones obtained in other works for the three considered configurations. The \* on Ref.[17] and on Ref. [35] means that the values presented in these references were obtained experimentally, while the others are theoretical predictions. We note that the theoretical results correspond to both the solution of the Wannier equation, quantum Monte Carlo simulations, and the solution of the Bethe-Salpeter equation, depending on the reference. We also stress the existence of a certain degree of dispersion among the results from different works. The † mark in Ref. [28] means we have used in our calculation the effective masses of this reference (our calculation of the exciton binding energy agrees well with that of this reference).

extremely similar to these ones, the only difference being the the smaller area across which the probability density extends, since the higher binding energy in these other two scenarios leads to more localized wave functions. Plotting these functions we have returned to the original  $x$  and  $y$  coordinates through the relation given in Eq. (4).

Finally we compute the mean value of  $x^2$  and  $y^2$  in the corrected exciton ground state. Although this may be a straightforward process, one aspect should be noted:

when evaluating the matrix elements one should only consider the contributions up to  $\beta^2$ , since otherwise one would be inconsistent with the potential expansion made

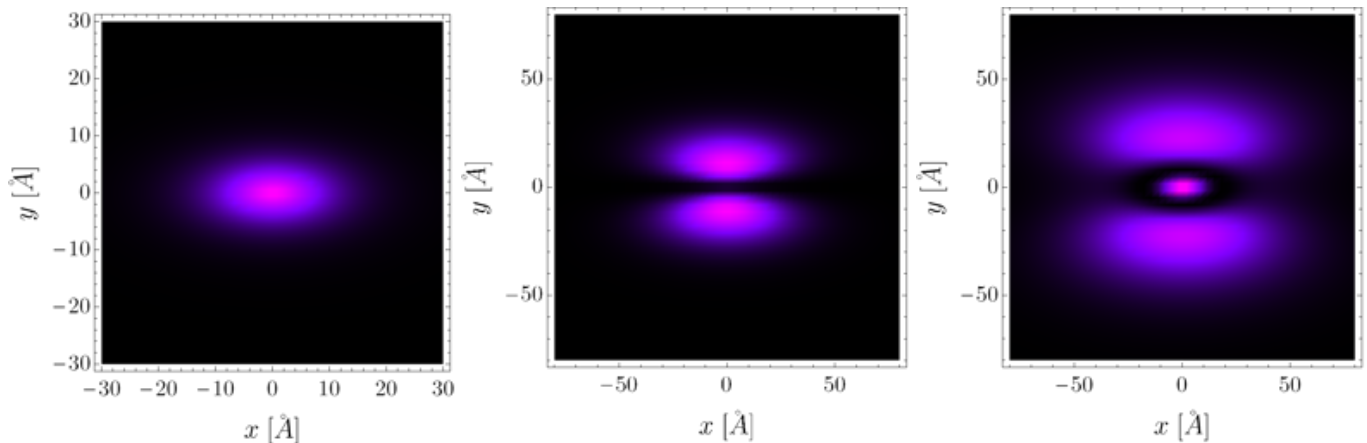


Figure 3. (Color online) Probability density (squared modulus of the corrected wave functions) for the  $1s$ ,  $2p_y$ , and  $2s$  exciton states of phosphorene encapsulated in hBN. These three states correspond to the three more tightly bound excitons. These plots emphasize the effect of the phosphorene anisotropic crystallographic structure on its excitons. When dealing with isotropic systems, such as the 2D hydrogen atom, the  $1s$  orbital presents a circular shape. This is not the case in phosphorene, where we see that for the  $1s$  state, what was once a circle, is now a disk stretched along the  $x$  direction. The same reasoning applies to the other two plots.

in the beginning of the text. The values we found for  $L_x = \sqrt{\langle x^2 \rangle_{gs}}$  and  $L_y = \sqrt{\langle y^2 \rangle_{gs}}$  for the three considered cases are presented in Table IV. There we see that  $L_x > L_y$  in agreement with the plot of Fig. 3. We also note that as the effect of dielectric screening diminishes, the values of both  $L_x$  and  $L_y$  decrease. This is a direct consequence of the connection between dielectric screening and the exciton binding energies, since as screening effects decrease, the binding energy grows, and the wave functions become more localized. We further note that the ratio between the values of  $L_x$  and  $L_y$  for freestanding phosphorene is in agreement with the one obtained in Ref.[27].

	in hBN ( $\kappa = 4.5$ )	on SiO <sub>2</sub> ( $\kappa = 2.4$ )	freest. ( $\kappa = 1$ )
$L_x$ (nm)	1.1	0.89	0.78
$L_y$ (nm)	0.54	0.44	0.39

Table IV. Computed values of  $L_x = \sqrt{\langle x^2 \rangle_{gs}}$  and  $L_y = \sqrt{\langle y^2 \rangle_{gs}}$  for phosphorene, using the *perturbed*  $1s$  wave function (*gs* stands for ground-state). It's possible to see that as  $\kappa$  decreases the values of  $L_x$  and  $L_y$  also decrease. This is a direct consequence of the higher localization of the exciton ground-state wave function. The abbreviation “freest.” stands for “freestanding”.

The perturbed binding energies of the three mostly bounded excitons are given in Table V. As expected, the mostly bounded states occur for the smallest value of the average dielectric function  $\kappa$ .

	$1s$	$2p_y$	$2s$
in hBN ( $\kappa = 4.5$ )	-256	-89	-61
on SiO <sub>2</sub> ( $\kappa = 2.4$ )	-449	-206	-149
freest. ( $\kappa = 1$ )	-825	-502	-405

Table V. *Perturbed* binding energies, up to order  $\beta^2$ , of the three mostly bounded excitonic states in the three experimental scenarios discussed in the text. All energies are in meV.

## V. CONCLUSIONS

In this work we have studied excitons in phosphorene in three different scenarios: encapsulated in hBN, on a substrate of SiO<sub>2</sub>, and freestanding.

Our approach to this problem hinges on a change of variable proposed by Rodin *et al.* in Ref. [22] that allowed us to treat the problem as an unperturbed Hamiltonian on which a perturbation, originated from the crystal structure anisotropy, acts. We then introduced a simple, yet effective, semi-analytical method that allowed us to solve the unperturbed part of our problem. Essentially the method requires the numerical determination of a set of coefficients  $c_j$  that define the wave-functions of the radial-symmetric problem once and for all; the rest of the calculations are analytical. To compute the effect of the crystal anisotropy characteristic of phosphorene we used perturbation theory. Because the wave-function of the excitons is analytical up to a set of numerical coefficients, we can give the excitonic wave function both in real and reciprocal spaces using simple analytical formulas. This will be important in future work in connection with the optical nonlinear properties of phosphorene [36, 37].

In possession of an analytical formula for the excitonic wave function, we computed the exciton binding energies in three different scenarios, having obtained -234, -428 and -799 meV for the ground state binding energy of phosphorene encapsulated in hBN, phosphorene on a SiO<sub>2</sub> substrate, and freestanding phosphorene, respectively. These values are in agreement with (within the same range) the values presented in other works using different numerical approaches. In all the considered cases the three more tightly bound excitons corresponded to  $1s$ ,  $2p_y$ , and  $2s$  states. We then plotted the probability density for different exciton states and, although not shown, we could have done the same in the reciprocal space, since the semi-analytical nature of our approach allows to pass between the real and reciprocal spaces with ease. We have also computed the characteristic length scales for the exciton ground state, having obtained  $L_x = 1.1$  nm and  $L_y = 0.53$  nm for freestanding phosphorene, and higher values for the other two studied cases. The difference between  $L_x$  and  $L_y$  reflects the crystal anisotropy that characterizes this 2D material. Finally we note that the method can be generalized to include the effect of electric (Stark effect [38]) and magnetic (magneto-optics) fields.

### ACKNOWLEDGMENTS

N.M.R.P. acknowledges support from the European Commission through the project “Graphene-Driven Revolutions in ICT and Beyond” (Ref. No. 785219), and

the Portuguese Foundation for Science and Technology (FCT) in the framework of the Strategic Financing UID/FIS/04650/2019. In addition, N. M. R. P. acknowledges COMPETE2020, PORTUGAL2020, FEDER and the Portuguese Foundation for Science and Technology (FCT) through projects PTDC/FIS- NAN/3668/2013 and POCI- 01-0145-FEDER-028114, and POCI-01-0145-FEDER- 029265 and PTDC/NAN-OPT/29265/2017, and POCI-01-0145-FEDER-02888. The authors acknowledge Paulo André Gonçalves and Ricardo Ribeiro for a critical reading of the manuscript.

### Appendix A: Kernel Expressions

In this appendix we present the analytical expressions for the Hamiltonian kernel  $H(\zeta_i, \zeta_j)$ , and the overlap kernel  $S(\zeta_i, \zeta_j)$ :

$$S(\zeta_i, \zeta_j) = 2\pi(\zeta_i + \zeta_j)^{-2-2|m|}\Gamma(2+2|m|) \quad (\text{A1})$$

$$H(\zeta_i, \zeta_j) = K(\zeta_i, \zeta_j) + V(\zeta_i, \zeta_j) \quad (\text{A2})$$

with

$$K(\zeta_i, \zeta_j) = \frac{\pi\zeta_i\zeta_j(\zeta_i + \zeta_j)^{-2-2|m|}(\mu_x + \mu_y)(\hbar c)^2\Gamma(2+2|m|)}{2\mu_x\mu_y} \quad (\text{A3})$$

and

$$V(\zeta_i, \zeta_j) = \frac{\pi\alpha\hbar c}{\kappa^2 r_0^2} \left\{ -2\kappa^3\Gamma(2|m|+3)(\zeta_i + \zeta_j)^{-2|m|-3} {}_3F_2 \left( 1, |m| + \frac{3}{2}, |m| + 2; \frac{3}{2}, \frac{3}{2}; -\frac{\kappa^2}{r_0^2(\zeta_i + \zeta_j)^2} \right) + r_0^3 2^{|m|+1} \cos(\pi|m|)\Gamma(|m|+1)^2 \left( \frac{\kappa}{r_0} \right)^{-2|m|} {}_2F_1 \left( |m| + 1, |m| + 1; \frac{1}{2}; -\frac{r_0^2(\zeta_i + \zeta_j)^2}{\kappa^2} \right) \right\} \quad (\text{A4})$$

- 
- [1] X. Ling, H. Wang, S. Huang, F. Xia, and M. S. Dresselhaus, PNAS **112**, 4523 (2015).
  - [2] K. S. Novoselov, A. K. Geim, S. V. Morozov, D. Jiang, Y. Zhang, S. V. Dubonos, I. V. Grigorieva, and A. A. Firsov, Science **306**, 666 (2004).
  - [3] M. J. Allen, V. C. Tung, and R. B. Kaner, Chem. Rev. **110**, 132 (2009).
  - [4] J. D. Caldwell, I. Aharonovich, G. Cassabois, J. H. Edgar, B. Gil, and D. Basov, Nature **4**, 552 (2019).
  - [5] G. Wang, A. Chernikov, M. M. Glazov, T. F. Heinz, X. Marie, T. Amand, and B. Urbaszek, Rev. Mod. Phys. **90**, 021001 (2018).
  - [6] A. Carvalho, M. Wang, X. Zhu, A. S. Rodin, H. Su, and A. H. C. Neto, Nat. Rev. Mat. **1**, 16061 (2016).
  - [7] J.-W. Jiang and H. S. Park, Nat. Comm. **5**, 4727 (2014).
  - [8] H. Yuan, X. Liu, F. Afshinmanesh, W. Li, G. Xu, J. Sun, B. Lian, A. G. Curto, G. Ye, Y. Hikita, *et al.*, Nat. Nano. **10**, 707 (2015).
  - [9] A. Rodin, A. Carvalho, and A. C. Neto, Phys. Rev. Lett. **112**, 176801 (2014).
  - [10] H. Asahina and A. Morita, J. of Phys. C: Sol. Stat. Phys. **17**, 1839 (1984).
  - [11] J. Qiao, X. Kong, Z.-X. Hu, F. Yang, and W. Ji, Nat. Comm. **5**, 4475 (2014).
  - [12] H. Liu, A. T. Neal, Z. Zhu, Z. Luo, X. Xu, D. Tománek, and P. D. Ye, ACS Nano **8**, 4033 (2014).



- [13] A. Castellanos-Gomez, L. Vicarelli, E. Prada, J. O. Island, K. Narasimha-Acharya, S. I. Blanter, D. J. Groenendijk, M. Buscema, G. A. Steele, J. Alvarez, *et al.*, 2D Materials **1**, 025001 (2014).
- [14] N. Gillgren, D. Wickramaratne, Y. Shi, T. Espiritu, J. Yang, J. Hu, J. Wei, X. Liu, Z. Mao, K. Watanabe, *et al.*, 2D Materials **2**, 011001 (2014).
- [15] S. P. Koenig, R. A. Doganov, H. Schmidt, A. Castro Neto, and B. Oezylmaz, App. Phys. Lett. **104**, 103106 (2014).
- [16] L. Li, Y. Yu, G. J. Ye, Q. Ge, X. Ou, H. Wu, D. Feng, X. H. Chen, and Y. Zhang, Nat. Nano. **9**, 372 (2014).
- [17] X. Wang, A. M. Jones, K. L. Seyler, V. Tran, Y. Jia, H. Zhao, H. Wang, L. Yang, X. Xu, and F. Xia, Nat. Nano. **10**, 517 (2015).
- [18] F. Ferreira and R. M. Ribeiro, Phys. Rev. B **96**, 115431 (2017).
- [19] J. Have, G. Catarina, T. G. Pedersen, and N. M. R. Peres, Phys. Rev. B **99**, 035416 (2019).
- [20] S. Rytova, Moscow University Physics Bulletin **22** (1967).
- [21] L. Keldysh, Sov. J. Exp. and Theor. Phys. Lett. **29**, 658 (1979).
- [22] A. Rodin, A. Carvalho, and A. C. Neto, Phys. Rev. B **90**, 075429 (2014).
- [23] J. C. G. Henriques, G. B. Ventura, C. D. M. Fernandes, and N. M. R. Peres, J. Phys.: Cond. Matt. **32**, 025304 (2019).
- [24] X. Yang, S. Guo, F. Chan, K. Wong, and W. Ching, Phys. Rev. A **43**, 1186 (1991).
- [25] J. J. Griffin and J. A. Wheeler, Phys. Rev. **108**, 311 (1957).
- [26] J. R. Mohallem, Zeitschrift für Physik D Atoms, Molecules and Clusters **3**, 339 (1986).
- [27] P. E. F. Junior, M. Kurpas, M. Gmitra, and J. Fabian, Phys. Rev. B **100**, 115203 (2019).
- [28] J.-H. Choi, P. Cui, H. Lan, and Z. Zhang, Phys. Rev. Lett. **115**, 066403 (2015).
- [29] M. V. der Donck and F. M. Peeters, Phys. Rev. B **98**, 235401 (2018).
- [30] R. J. Hunt, M. Szyniszewski, G. I. Prayogo, R. Maezono, and N. D. Drummond, Phys. Rev. B **98**, 075122 (2018).
- [31] A. Chaves, T. Low, P. Avouris, D. Çakır, and F. Peeters, Phys. Rev. B **91**, 155311 (2015).
- [32] S. Arra, R. Babar, and M. Kabir, Phys. Rev. B **99**, 045432 (2019).
- [33] V. Tran, R. Fei, and L. Yang, 2D Materials **2**, 044014 (2015).
- [34] V. Tran, R. Soklaski, Y. Liang, and L. Yang, Phys. Rev. B **89**, 235319 (2014).
- [35] G. Zhang, A. Chaves, S. Huang, F. Wang, Q. Xing, T. Low, and H. Yan, Sci. Adv. **4**, eaap9977 (2018).
- [36] T. G. Pedersen, Phys. Rev. B **95**, 235419 (2017).
- [37] F. Hipolito and T. G. Pedersen, Phys. Rev. B **97**, 035431 (2018).
- [38] L. S. R. Cavalcante, D. R. da Costa, G. A. Farias, D. R. Reichman, and A. Chaves, Phys. Rev. B **98**, 245309 (2018).